Available online at www.sciencedirect.com

jmr&t
Journal of Materials Research and Technology

journal homepage: www.elsevier.com/locate/jmrt

Numerical simulation and experimental investigation of the laser cladding processes of Ti6Al4V with coaxial shroud protection

Peijie Lyu [a], *Peifeng Li* [b], *Kaiyong Jiang* [a,*]

[a] *Fujian Key Laboratory of Special Energy Manufacturing, Xiamen Key Laboratory of Digital Vision Measurement, Huaqiao University, Xiamen 361021, China*

[b] *James Watt School of Engineering, University of Glasgow, Glasgow, G12 8QQ, United Kingdom*

ARTICLE INFO

Article history:
Received 4 May 2023
Accepted 16 August 2023
Available online 21 August 2023

Keywords:
Laser cladding
Coaxial shroud protection
Computational fluid dynamics (CFD)
Ti6Al4V (TC4)
Electron backscattering diffraction (EBSD)

ABSTRACT

Laser cladding with coaxial shroud protection offers the possibility to process reactive metals in an open environment. The numerical analysis was performed on the thermal field and dynamics of molten pool with the aim of clarifying the mechanism of the complex effects of the applied extra shielding gas on the resultant microstructure and surface quality of cladding layers of Ti6Al4V. A three-dimensional (3D) computational fluid dynamics (CFD) model was first developed to investigate the extra shielding gas effect on the molten pool. The simulation shows that the extra shielding gas influences both the surface and internal flow field characteristics of the molten pool. The predicted solidification parameters imply fully columnar microstructure in the entire cladding layer. Comparative analysis was then carried out between the numerical simulation and experiments. The electron backscattering diffraction (EBSD) examination reveals that the high cooling rate due to the extra shielding gas inhibits the formation of grain boundary α phase and simultaneously refines the microstructure. The extra shielding gas reduces the surface roughness of cladding layers, and its bunching effect improves the powder utilization. The multi-track cladding experiments reveal that the extra shielding gas can effectively suppress crack formation with a large overlap ratio. This study provides a better understanding of the effect of extra shielding gas flow on molten pool, which helps control and improve the quality of cladding layers.

1. Introduction

Laser cladding, a promising additive manufacturing (AM) technique is widely used in industries due to its high energy utilization, low dilution, flexibility and portability [1]. The coaxial nozzle has the functions of emitting laser and adding materials. The laser beam melts the object surface, creating a molten pool to which additive materials such as metal powders or wires are added and then immediately solidify to form a new metallurgical layer [2–4].

Many complex driving forces act on the molten pool simultaneously, which are mainly caused by temperature gradients and/or surface active element concentration [5].

* Corresponding author.
E-mail address: jiangky@hqu.edu.cn (K. Jiang).

https://doi.org/10.1016/j.jmrt.2023.08.163

However, the rapid melting-solidification and high temperature make it difficult to observe and detect the molten pool state. Therefore, accurate numerical simulation is an effective tool to reveal some phenomena. Yang et al. [6] developed a three-dimensional (3D) numerical model based on the commercial software FLOW-3D to reveal the dynamics of the molten pool during metal AM with ultrasound. Siao and Wen [7] investigated the effect of Marangoni stress on the molten pool by a 3D numerical model, and the results show that the Marangoni stress is the dominant factor in the molten pool motion. Zhang et al. [8] developed a computational fluid dynamics (CFD) model and found that the flow dynamics of the molten pool has a remarkable influence on the heat and mass transfer mechanisms. Li et al. [9] studied the relationship between the microstructure and the molten pool by considering surface tension and buoyance force using a coupled multi-physics numerical model. Arrizubieta et al. [10] used a numerical model to study the effect of the thermal field on dendrite arm spacing and mechanical properties in laser cladding. However, there is a lack of reports on the effect of shielding gas flow on the molten pool. In some literatures [11–14] the shielding gas was considered to be relatively small, and its role was directly disregarded.

Coaxial shroud protection is an auxiliary technology that offers the possibility to process reactive metals in an open environment [15,16]. Compared with as-received cladding conditions, the extra shielding gas flow injected from the coaxial shroud not only changes the powder-gas flow field characteristics, but also directly affects the state and formation of molten pool. Furthermore, the high speed gas flow can change the surface heat dissipation from free convection to forced convection, thus influencing the solidification parameters. Chen et al. [17] and Song et al. [18] treated the shielding gas pressure as a Gaussian distribution over the free surface of the molten pool. Khamidullin et al. [19] derived an expression for the slip velocity between the gas and liquid phases. However, there is no discussion of how the shielding gas affects the thermal field of the molten pool. Moreover, the shielding gas pressure does not necessarily satisfy the Gaussian distribution due to its small size.

Ti6Al4V as a workhorse alloy in Ti is widely used in AM due to the excellent comprehensive properties by the coexistence of α+β phases at room temperature [20]. During multi-track cladding, the internal stress concentration as a result of multiple heating and cooling cycles tends to cause cracks. The cracks are one of the most frequently formed defects that reduce the quality of cladding layers. The classic solution is to preheat the substrate to balance the internal stress expansion [21]. However, it is not possible to preheat all substrates in practical open processing situations. Therefore, the control of the temperature field provides an alternative solution [22,23]. At the same time, the powder utilization rate should also be considered in large area multi-layer cladding.

There is much less research, however, dedicated to understanding how the gas interacts with the molten pool. In this study a 3D CFD model using the Volume-of-Fluid (VOF) method was developed in the commercial software FLUENT to simulate the laser cladding process. The surface tension, Marangoni stress, gravity force, buoyance force and Darcy force were all considered to describe the mass and heat transfer of the molten pool. In particular, the interaction of extra shielding gas with the molten pool was implemented in two aspects. For momentum, the impulse boundary condition was introduced. For energy, the gas forced convection condition was used to represent the rapid heat dissipation. The simulated flow characteristic and solidification parameters of the molten pool were analyzed. Microstructure, crystallographic textures and quality of cladding layer were experimentally measured and combined with the simulation results to provide in-depth analysis. This study reveals the effect of extra shielding gas flow on molten pool and gives a better understanding of the coaxial shroud protection technology.

2. Mathematical models

In this research, molten pool fluid flow and heat transfer were calculated under different conditions through the governing equations of mass, momentum and energy conservation. The VOF method was used to track the free surface of molten pool. Some assumptions were made to simplify the model as follows. 1) Laser-powder interaction is ignored. 2) Powders become liquid when they are in the molten pool, i.e., the temperature of adding material reaches the liquidus temperature. 3) The flow in the molten pool is laminar and incompressible. 4) Evaporation is not considered due to the temperature below the evaporation point; 5) The impact of powders on molten pool is neglected; 6) Carrier gas, central shielding gas and extra shielding gas are linearly superimposed on the free surface.

2.1. Governing equations

The governing equations can be defined as

$$\frac{\partial \rho}{\partial t} + \nabla \cdot (\rho \vec{v}) = 0 \tag{1}$$

$$\frac{\partial}{\partial t}(\rho \vec{v}) + \nabla \cdot (\rho \vec{v}\,\vec{v}) = -\nabla p + \nabla \cdot [\mu(\nabla \vec{v} + \nabla \vec{v}^{T})] + \rho \vec{g} + S_F \tag{2}$$

$$\frac{\partial}{\partial t}(\rho H) + \nabla \cdot (\rho \vec{v} H) = \nabla \cdot (k \nabla T) + S_E \tag{3}$$

$$\frac{\partial \alpha}{\partial t} + \nabla \cdot (\alpha \vec{v}) = 0 \tag{4}$$

where ρ, μ, k and ∇T are the local density, viscosity, heat conduction coefficient and the temperature gradient respectively, $\vec{v}$ is the velocity vector, H is the enthalpy, S_F and S_E are the source terms of momentum and energy, and α is the volume fraction. $\alpha = 1$ is defined for the gas phase, $\alpha = 0$ for the solid or liquid (SorL) phase, and $0 < \alpha < 1$ for the free surface between the gas and SorL phases.

2.2. Solid-liquid phase change

During the laser cladding process, the first phase transformation is that the solid (powders) is melted to the liquid in molten pool. Then, the molten pool solidifies to a cladding layer. The laser cladding process is accompanied by rapid

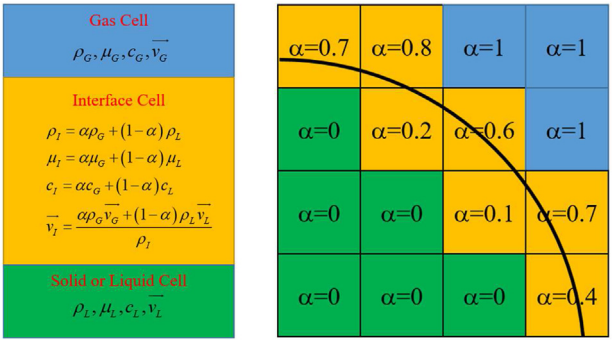

Fig. 1 – Physical properties of calculation domain.

energy transfer within and between the phases. According to Enthalpy-Porosity model, a liquid fraction β is defined to identify the pure solid phase, pure liquid phase and mushy zone.

$$\beta = \begin{cases} 0 & T < T_S \\ \dfrac{T - T_S}{T_L - T_S} & T_S \le T \le T_L \\ 1 & T_L < T \end{cases} \tag{5}$$

The total enthalpy of the material H is regarded as $H = cT + \beta L$, where the c is the specific heat, and the L is the latent heat of liquefaction. T_S and T_L are the solidus and liquidus temperatures, respectively. Therefore Eq. (3) can be written as

$$\begin{cases} \dfrac{\partial(\rho cT)}{\partial t} + \vec{v}\cdot\nabla(\rho cT) = \nabla\cdot(k\nabla T) & T < T_S \\ \dfrac{\partial(\rho cT)}{\partial t} + \vec{v}\cdot\nabla(\rho cT) = \nabla\cdot(k\nabla T) - \dfrac{\partial(\rho\beta L)}{\partial t} - \vec{v}\cdot\nabla(\rho\beta L) & T_S < T < T_L \\ \dfrac{\partial(\rho cT)}{\partial t} + \vec{v}\cdot\nabla(\rho cT) = \nabla\cdot(k\nabla T) - \dfrac{\partial(\rho L)}{\partial t} - \vec{v}\cdot\nabla(\rho L) & T_L < T \end{cases} \tag{6}$$

2.3. The VOF method and material properties

As mentioned above, the VOF method was used to track the free surface between the SorL phase and gas phase. Therefore, the physical boundary of free surface such as laser heat input, surface thermal convection and radiation, surface tension, Marangoni effect and gas impulse effect should be added to the cell with $0 < \alpha < 1$. For the given volume and space position of mesh, the physical properties of interface elements are related to the volume fraction of gas and SorL phase [24], as shown in Fig. 1. The main physical properties of the material (see Table 1 and Fig. 2) were calculated by the commercial software JMatPro. In the model, the substrate and as-solidified cladding track were regarded as a fluid phase with high viscosity [25].

2.4. Energy conditions

On the free surface, heat transfer dominated by laser heat (q_{Las}) input, heat convection (q_H) and heat radiation (q_T) replaces heat conduction in a pure phase. Therefore, the heat conduction in energy equation can be deduced as

$$-k\nabla T = q_{Las} + q_H + q_T \tag{7}$$

where the top-hat laser heat is defined by $q_{Las} = \frac{\eta_{Las}P_{Las}}{\pi r^2}$, heat convection is expressed as $q_H = -h_c(T - T_0)$ and heat radiation is written as $q_T = -\sigma_B\varepsilon(T^4 - T_0^4)$. The final energy equation on the free surface can be described as

$$\frac{\partial(\rho cT)}{\partial t} + \vec{v}\cdot\nabla(\rho cT) = \nabla\cdot\left(\frac{\eta_{Las}P_{Las}}{\pi r^2} - h_c(T - T_0) - \sigma_B\varepsilon\left(T^4 - T_0^4\right)\right) - \frac{\partial(\rho L)}{\partial t} - \vec{v}\cdot\nabla(\rho L) \tag{8}$$

while the free surface beyond the laser irradiation range can be written as

$$\frac{\partial(\rho cT)}{\partial t} + \vec{v}\cdot\nabla(\rho cT) = \nabla\cdot\left(-h_c(T - T_0) - \sigma_B\varepsilon\left(T^4 - T_0^4\right)\right) - \frac{\partial(\rho L)}{\partial t} - \vec{v}\cdot\nabla(\rho L) \tag{9}$$

where η_{Las} is the laser energy efficiency. The laser absorptivity of the TC4 substrate (Fig. 3) was measured in a spectrophotometer (LAMBDA 1050, Perkin Elemer, China) with 150 mm integrating sphere. The absorptivity of 57.8% was used for the laser wavelength 1064 nm in this study (Table 1). P_{Las} is the laser power, r is the laser radius, ε is the emissivity, σ_B is the

Table 1 – Physical properties of materials used in the model.

Physical variables (Unit)	Symbol	Value	Reference
Solidus temperature (K)	T_S	1928	JMatPro
Liquids temperature (K)	T_L	1987	JMatPro
Density (kg·m^{-3})	ρ	4510	[26]
Thermal conductivity (W·m^{-1}·K^{-1})	k	Fig. 2(b)	JMatPro
Viscosity (mPa·s)	μ	Fig. 2(c)	JMatPro
Melting latent heat (J·kg^{-1})	L	3.48e5	JMatPro
Surface tension (mN·m^{-1})	σ	Fig. 2(d)	JMatPro
Thermal expansion coefficient (K^{-1})	λ	1.2e-5	[27]
Specific heat (J·kg^{-1}·K^{-1})	c	Fig. 2(a)	JMatPro
Convective heat transfer coefficient (W·m^{-2}·K^{-1})	h_c	9.0 and 65.5	[28,29]
Surface radiation emissivity	ε	0.35	[30]
Stefan-Boltzmann constant	σ_B	5.67e-8	[30]
Initial temperature (K)	T_0	300	–
Laser absorptivity (%)	η_{LAS}	57.8	Measurement

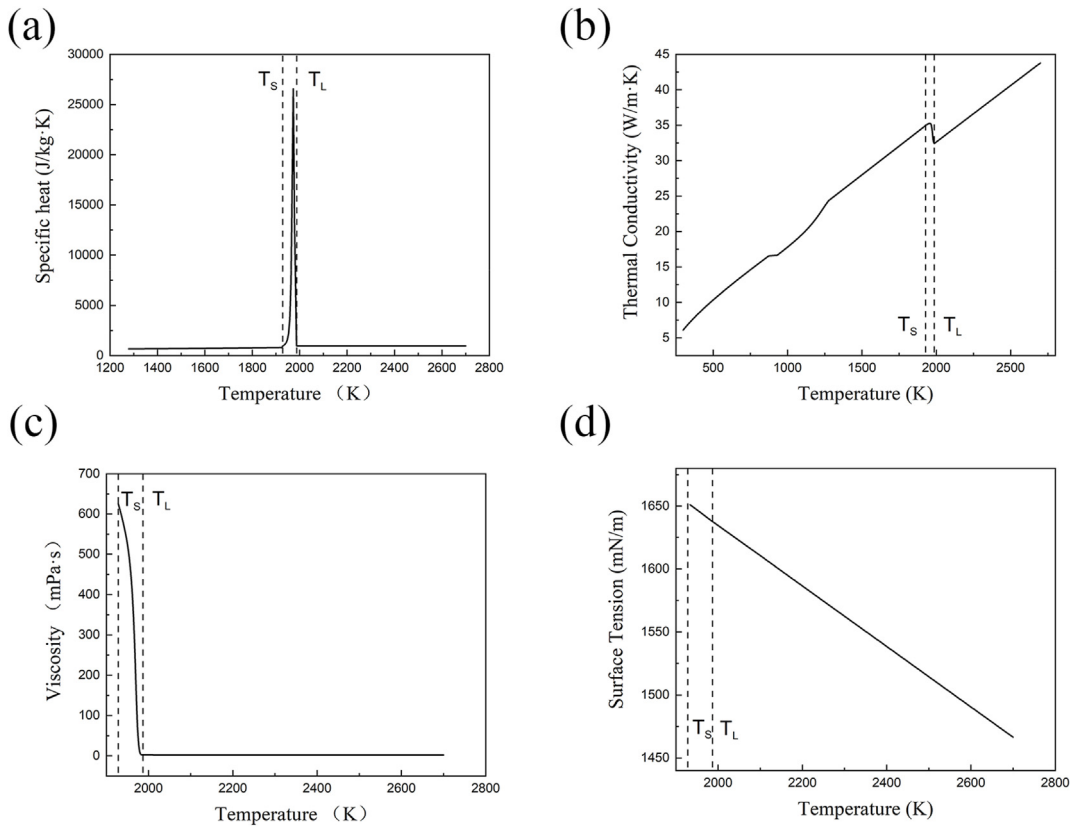

Fig. 2 – Temperature-dependent physical properties calculated by JMatPro: (a) specific heat; (b) thermal conductivity; (c) viscosity; (d) surface tension.

Boltzmann coefficient, T_0 is the ambient temperature, and h_c is the heat convection coefficient. When the gas effect is considered, the free convection changes to forced convection. According to the literatures [28,29], the free convection coefficient and gas forced convection coefficient used in the simulation are 9 and 65.5 W m^{-2} K^{-1}, respectively.

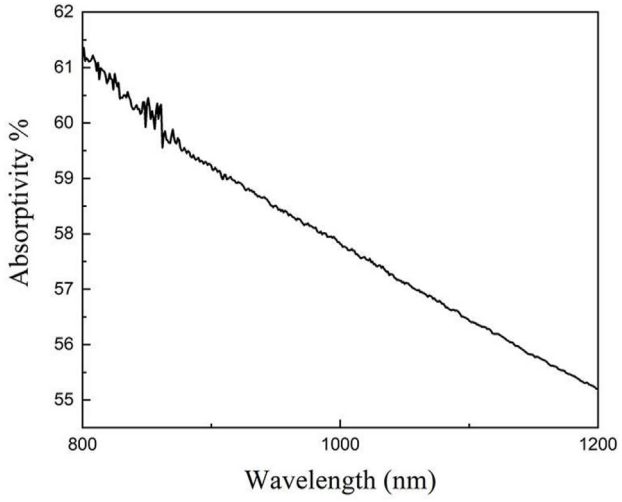

Fig. 3 – The laser absorptivity of substrature from 900 to 1200 nm of wavelength.

2.5. *Momentum conditions*

The momentum source term S_F in Eq. (2) includes the body force f_{body} and surface force $f_{surface}$, and can be expressed as follows,

$$S_F = f_{body} + f_{surface} = \left(f_{Bouyancy} + f_{Darcy}\right) + \left(f_{Surface\ Tension} + f_{Marangoni} + f_{Gas}\right) \quad (10)$$

where the body force includes Buoyance force $f_{Bouyance}$ and Darcy force f_{Darcy}, and the surface force includes surface tension $f_{Surface\ Tension}$, Marangoni stress $f_{Marangoni}$ and gas force f_{Gas} Since the temperature is below the vaporization temperature, the recoil pressure is ignored. The Buoyance force is based on the Boussinesq model with a constant density:

$$f_{Bouyancy} = -\rho_0 \lambda (T - T_0) g \quad (11)$$

where λ is the thermal expansion coefficient, and ρ_0 is the constant density of the flow. The mushy zone was treated as a porous medium. The momentum sink due to porosity can be expressed as

$$f_{Darcy} = \frac{(1-\beta)^2}{(\beta^3 + \varepsilon)} A_{mush} (\vec{v} - \vec{v_e}) \quad (12)$$

where β is the liquid volume fraction, ε is a very small number (0.001) that makes division meaningful, A_{mush} is the mushy constant with the default value 10^5, and $\vec{v_e}$ is the pull velocity.

The surface tension and Marangoni stress are rewritten as volumetric force with the continuum surface force (CSF) model [31].

$$f_{Surface\ Tension} = \sigma \cdot \kappa \cdot \vec{n} \cdot |\nabla\alpha| \cdot \frac{2\rho_{surface}}{\rho_L + \rho_G} \tag{13}$$

$$f_{Marangoni} = \frac{\partial\sigma}{\partial T} \cdot \nabla_s T = \frac{\partial\sigma}{\partial T} \cdot (\nabla T - (\nabla T \cdot \vec{n})\vec{n}) \cdot |\nabla\alpha| \cdot \frac{2\rho_{surface}}{\rho_L + \rho_G} \tag{14}$$

where σ is the surface tension coefficient, $\vec{n}$ is the normal unit vector, $\kappa = -\nabla \cdot \vec{n}$ is the mean curvature of molten pool surface, $|\nabla\alpha|$ is the Delta function to transfer surface force to volumetric force, $\nabla_s T$ is the surface temperature gradient, and $\frac{2\rho_{surface}}{\rho_L+\rho_G}$ is a redistributing coefficient for smeared force toward a heavier phase [32].

Although the molten pool lasts for a very short time, it is affected by very complex gas forces. This was usually ignored in the previous studies. As shown in Fig. 4(a), the carrier gas, central shielding gas and extra shielding gas impact directly on the molten pool. The carrier gas and extra shielding gas are considered to be ideal gases perpendicular to the free surface, while the central shielding gas can be decomposed into tangential ($F_{Tangential} = F_{Central\ shielding\ gas} \cdot \cos\alpha$) and normal ($F_{Normal} = F_{Central\ shielding\ gas} \cdot \sin\alpha$) directions as shown in Fig. 4(b). Though the tangential force increases with α from top to bottom along the liquid surface, the carrier gas and extra shielding gas are so large that the tangential force can be negligible and only the normal force is considered. The carrier gas, central shielding gas and extra shielding gas are linearly superimposed on the free surface.

$$f_{Gas} = f_{Carried\ gas} + f_{Central\ shielding\ gas} + f_{Extra\ shielding\ gas} \tag{15}$$

According to the conservation of gas impulse, the action of gas can be written as

$$F \cdot \Delta t = m_G \vec{v}_{END} - m_G \vec{v}_G \tag{16}$$

where Δt is the duration time of the gas action, $\vec{v}_G$ is the gas velocity before impacting the free surface and $\vec{v}_{END}$ is the final velocity. Assuming that the gas velocity to the surface decreases to zero ($\vec{v}_{END} = 0$), the gas force can be described as

$$F = \frac{-m_G \vec{v}_G}{\Delta t} \tag{17}$$

where the quantity of gas m_G can be defined by

$$m_G = \rho_G \cdot V = \rho_G \cdot \vec{v}_G \cdot \Delta t \cdot \Delta S \tag{18}$$

where V is the volume of gas, ΔS is the free surface area in a cell. Finally the momentum source of gas for each cell can be written as

$$f_{Gas} = \rho_G \cdot \vec{v}_G^2 \cdot \Delta S \cdot |\nabla\alpha| \cdot \frac{2\rho_{surface}}{\rho_L + \rho_G} \tag{19}$$

2.6. Material addition

In this research, a coaxial laser head with four powder exits was used. The jet stream is considered as a turbulent jet stream, i.e., the powder flux satisfies the Gaussian distribution on the section of focus plane [33,34]. The strategy of adding powders is to assign material properties to the volume-filled mesh. Building the coordinates of XY plane with powder focus as center at upper substrate on the section perpendicular to the scanning direction, the number of filled volumes for each column element can be written as [10]:

$$Ele = 2 \cdot \frac{\eta_p \cdot \dot{m} \cdot \Delta t}{\Delta z \cdot \rho \cdot \pi \cdot r_p^2} \exp\left(-2 \cdot \frac{x^2 + y^2}{r_p^2}\right) \tag{20}$$

where $\dot{m}$ is the powder feeding rate, and the experimental value of $\dot{m} = 0.67$ g/s is taken. η_p is the powder utilization efficiency, increased by 10.37% as bunching effect of shielding gas [16]. Δz is the height of the element, Δt is the fixed time step in this simulation model, and r_p is the powder stream radius which is equal to the laser radius. Table 2 presents the process parameters in detail. When the filled fraction of an element equal to unity, namely, $\alpha = 1$, it is assigned the physical properties of metallic material. The top element of each element column is treated as free surface which $0 < \alpha < 1$. The cell is assigned the properties of ideal gas when $\alpha = 0$.

This simulation was carried out in FLUENT, and the material properties, boundary conditions and value extraction were realized by user-defined function (UDF) with the C language. The pressure implicit with splitting of

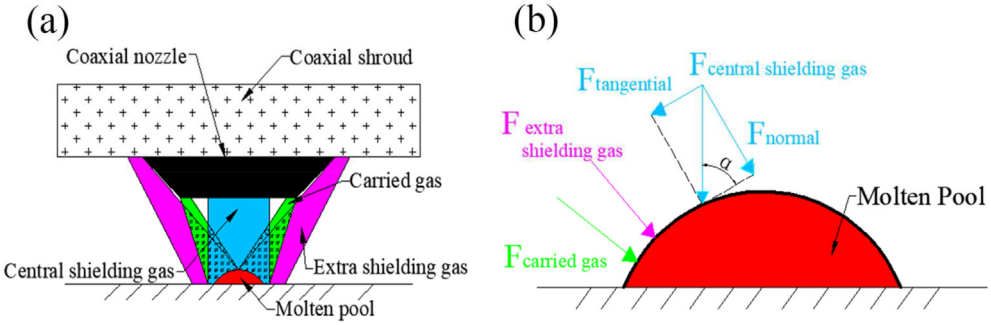

Fig. 4 – Analysis of flattening effect on the surface of the molten pool: (a) illustration of the action of gases on molten pool; (b) the gas forces acting on the molten pool.

Table 2 – Material addition process parameters applied in this study.

Parameters (unit)	Symbol	Value
Powder feeding rate (g/s)	$\dot{m}$	0.67
Powder utilization efficiency (%)	η_p	80.5 [35]/88.8
Height of element (mm)	Δz	0.02
Time step (s)	Δt	0.01
Powder stream radius (mm)	r_p	2

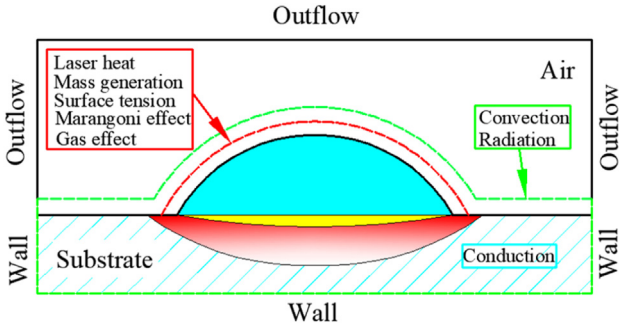

Fig. 5 – The applied boundary conditions of the model.

operators (PISO) method was used to solve the pressure-velocity coupling. The Geo-Reconstruct scheme was employed to calculate the volume fraction. The second order upwind scheme was used to discretize the temperature and velocity fields. All the applied boundary conditions are shown in Fig. 5.

3. Experimental setup and materials

3.1. Experimental setup

The laser cladding setup consists of a laser diode module (LDM) semiconductor laser (LDM-2500, LaserLine, German) equipped with 6-axis robot (IRB4600, ABB, Switzerland), a powder feeding system (RC-PGF-D-2, Nanjing Zhongke Raycham Laser Technology Co., Ltd.), a chiller system (MCWL-70DTR-04X1-3385, Sanhe City Tongfei Refrigeration Equipment Co., Ltd., China), and a self-designed three-layer annual coaxial shielding shroud (TACS), as shown in Fig. 6. The pure Argon (99.99%) was used as the protective gas. A gas flowmeter (LZT M – 6, Jiangsu Kenchuang Instrument Co., Ltd.) was used to control the gas flowrate. The optimized value of 30L/min that was determined in the previous work [16] was used for the flowrate of extra shielding gas for each channel. The parameters for the laser cladding experiments are listed in Table 3. The geometry and surface roughness of cladding samples were measured in a high-resolution 3D optical profiler (KEYENCE, VR5000, Japan). The chromel-alumel (K-type) thermocouples were used to measure the temperature history of different locations on the substrate during laser cladding. Scanning electron microscope (SEM, JSM-IT500LA, Japan) equipped with an energy dispersive spectroscopy (EDS) was used to observe the powders and the microstructure of

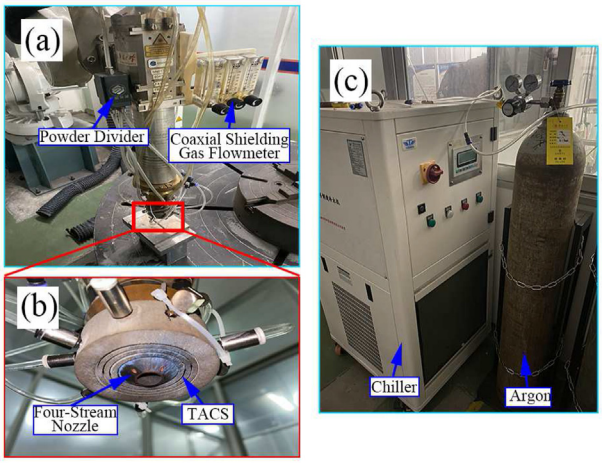

Fig. 6 – The laser cladding experimental setup: (a) the laser nozzle, (b) assembly of the TACS and (c) the chiller and argon.

cladding samples. The EBSD detector was used to examine the grain morphology and orientation in the selected area of the samples.

3.2. Materials

The gas-atomized pre-alloyed TC4 powders (powder diameter 45–150 μm, Avimetal Powder Metallurgy Technology Co., Ltd., China) were used in this study. The chemical composition (wt. %) of powders is 6.06 Al, 4.04 V, 0.03 Fe and balanced Ti. The TC4 substrates of 100 × 100 × 10 mm were polished with sandpaper and cleaned with alcohol before laser cladding (see Fig. 7). The cross-section of cladding samples was polished and etched using the Kroll's reagent [36] (2–3% HF, 4–5% HNO_3, 92–94% H_2O) before the SEM observations.

4. Results and discussion

4.1. Transient velocity of molten pool

The surface tension temperature coefficient ($\partial\sigma/\partial T$) determines the fluid flow direction on the molten pool surface [13]. When $\partial\sigma/\partial T > 0$, the liquid metal flows from the periphery to the center of the molten pool, forming an inward flow and thus leading to a deeper and narrower cladding layer. When $\partial\sigma/\partial T < 0$, the liquid metal flows from the center to the periphery of the molten pool, forming an outward flow and thus leading to a wider and shallower cladding layer.

Fig. 2(d) shows that the surface tension of liquid TC4 decreases with increasing temperature, i.e., $\partial\sigma/\partial T < 0$. In combination with the Marangoni stress which is related to the surface temperature gradient $\nabla_s T$, the liquid tends to flow from the low surface tension region to the relatively high surface tension region [37] and forms an outward flow. The vortex-like flow velocity streamlines as shown in Fig. 8(b) are similar to the X-ray observations by Guo et al. [38]. This vortex-like flow facilitates the heat transfer in the molten pool to obtain a uniform heat distribution.

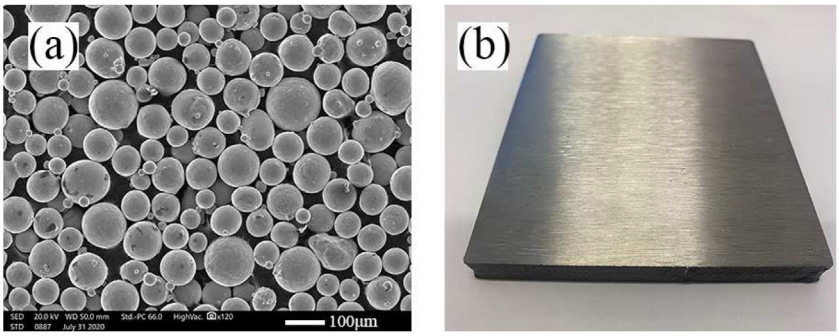

Fig. 7 – (a) SEM observations of TC4 powders and (b) TC4 substrate.

Table 3 – Main parameters for experiments.

Parameters (unit)	Symbol	Value
Laser power (W)	P	1401
Scanning speed (mm/s)	V_{ss}	6
Carried gas flowrate (L/min)	FR_1	10
Central shielding gas flowrate (L/min)	FR_2	18
Extra shielding gas flowrate (L/min)	FR_3	30

Although the molten pool exists for a very short time, its motion is intense due to various complex driving forces [39]. Among these factors, the flattening effect of shielding gas is rarely considered in the existing literature [25,40,41]. In this study, the extra shielding gas was considered as gas impulse condition on the molten pool surface. The following analysis was performed on the X-Z and Y-Z planes indicated in Fig. 8(a).

Fig. 9 shows the molten pool state on the X-Z plane at different time under two conditions. Conditions Item 1 and Item 2 are without and with extra shielding gas, respectively. When t = 0.1s, the molten pool behind the laser radiation zone (right side) solidifies faster as the laser source moves along the positive direction of the X-Axis (see Fig. 9(a) - Item 1 and 2). When t = 0.3s, the maximum velocity in the molten pool without extra shielding gas effect is on the upper of the molten pool which is mainly dominated by temperature gradient between the molten pool and as-solidified track (see Fig. 9(b) - Item 1 and Item 2). When t = 0.5s, only the vortex flow at the rear of the molten pool forms when the extra shielding gas is not considered (see Fig. 9(c) - Item 1). However, the vortex flow does not form even if the velocity near the surface of molten pool is increased when the extra shielding gas is applied (see Fig. 9(c) - Item 2). When t = 0.7s, two vortex flows form, and the molten pool is in a steady state (see Fig. 9(d) - Item 1). However, the molten pool is deformed by the extra shielding gas, i.e. the space is narrowed, resulting in no vortex formation (see Fig. 9(d) - Item 2). To sum up, though the extra shielding gas increases the velocity near the molten pool surface, it also inhibits the formation of internal vortices in the scanning direction by shaping molten pool space.

Fig. 10 shows the molten pool state on the Y-Z plane. The area of the molten pool on the Y-Z plane becomes larger due to the bunching effect of shielding gas, implying an increased powder utilization rate. The velocity near the molten pool surface also increases under the extra shielding gas effect. The simulation results are in good agreement with the experiments.

4.2. *Thermal field of cladding process*

To validate the CFD model, the temperature history was experimentally measured by the k-type thermocouples under different convection conditions and compared with the numerical results. Three thermocouple test points P1, P2 and P3 were placed on the substrate as shown in Fig. 11. Error percentage between the measurement and simulation results can be calculated by [42].

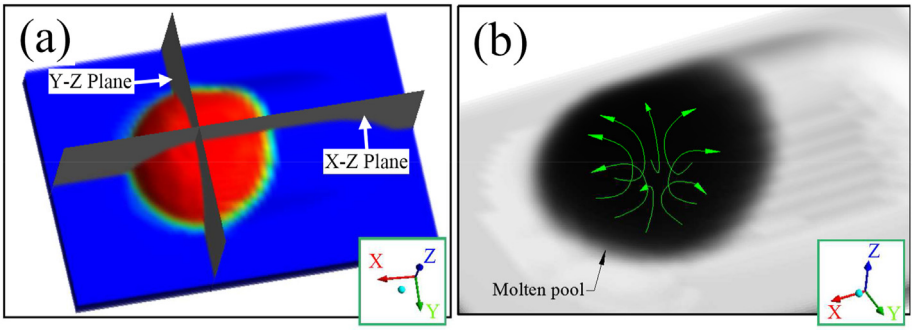

Fig. 8 – The schematic of simulated molten pool: (a) the X-Z and Y-Z plane diagram, (b) the outward flow diagram in the molten pool.

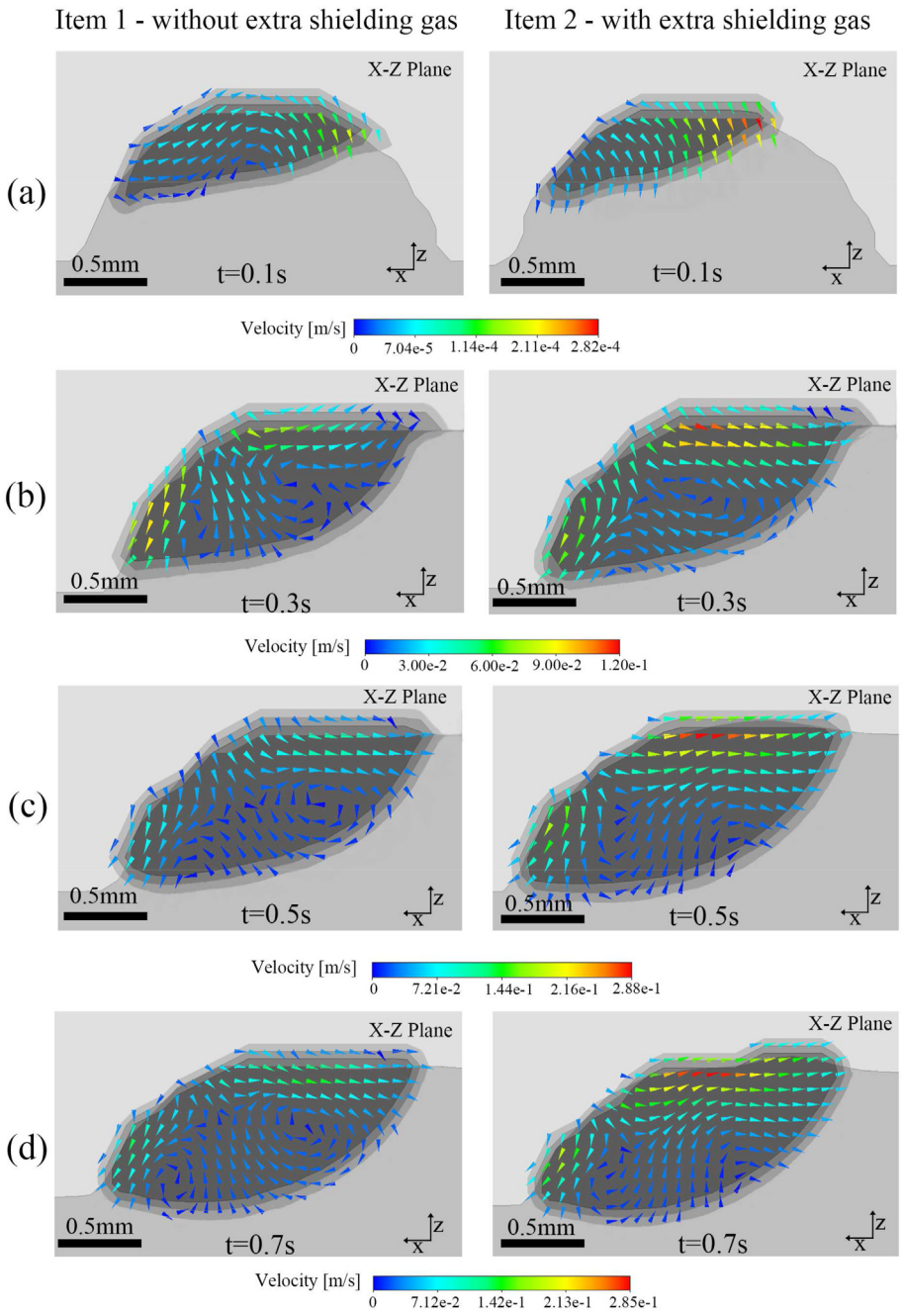

Fig. 9 – The simulated velocity field on the X-Z Plane of the molten pool at 0.1s, 0.3s, 0.5s and 0.7s. Item 1 and Item 2 is without and with considering the flattening effect of shielding gas, respectively.

$$\%Error = \frac{100\sum_{i=1}^{n}\left|\left[(T_m)_i - (T_s)_i\right]/(T_m)_i\right|}{n} \quad (21)$$

where n is the total number of time increments in a simulation, T_m is the measured temperature and T_s is the simulated temperature.

Fig. 12 shows the numerical and measurement results of a single cladding layer without considering gas forced convection heat dissipation. The temperature increases sharply when the laser just approaches, and the temperature immediately starts to cool down as the laser moves away. The numerical results agree well with the measured data for the feature of rapid heating and cooling at the three measurement locations. The overall error percentage of P1, P2 and P3 are 4.93%, 5.63% and 6.27%, respectively. The temperature results under gas forced convective heat dissipation condition are shown in Fig. 13. The peak temperature of all three points reduces due to abundant heat loss by gas forced convective heat dissipation in surface. The measured temperature history of P1 and P2 has a V-shaped valley at the cooling stage after the peak temperature. This is because as the extra coaxial shielding gas moves away, the dominant factor of heat

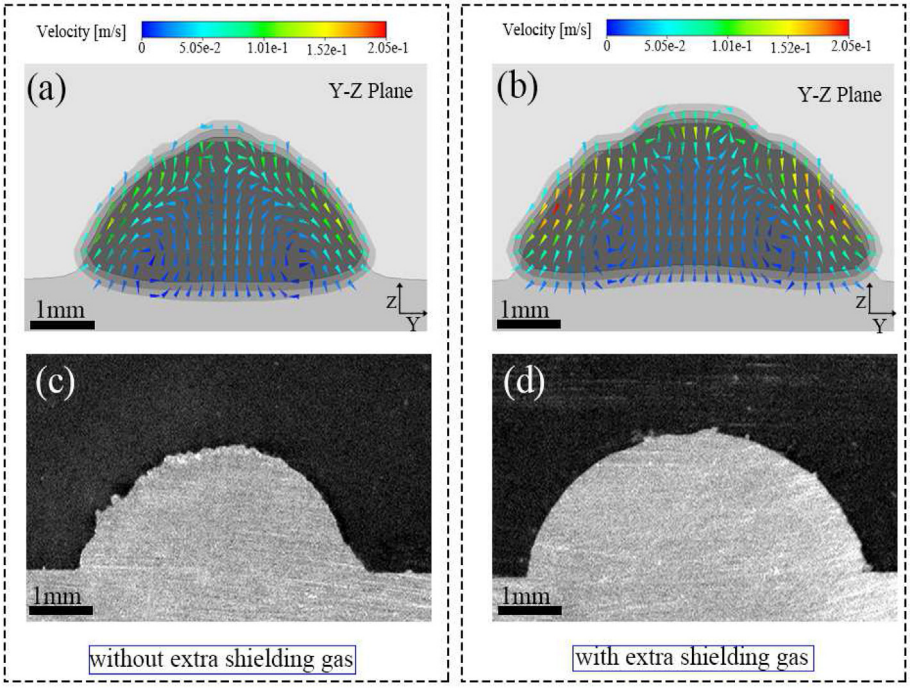

Fig. 10 – The simulation and experimental results on the Y-Z Plane: (a), (c) without extra shielding gas; (b), (d) with extra shielding gas.

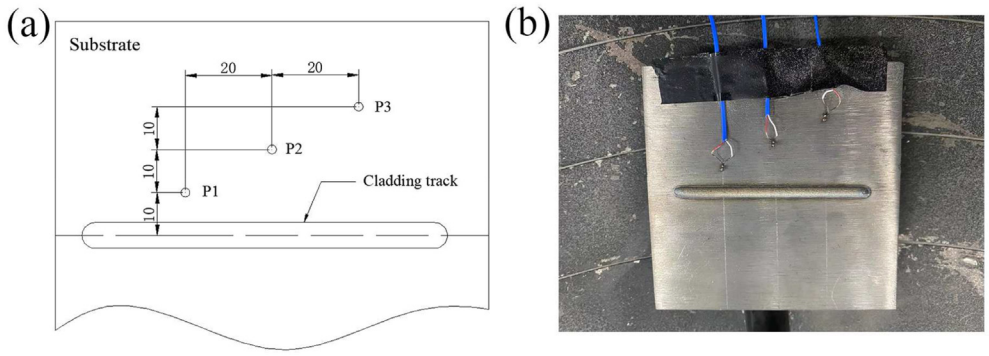

Fig. 11 – (a) Positions of thermocouples on substrate. (b) The schematic of real experimental test.

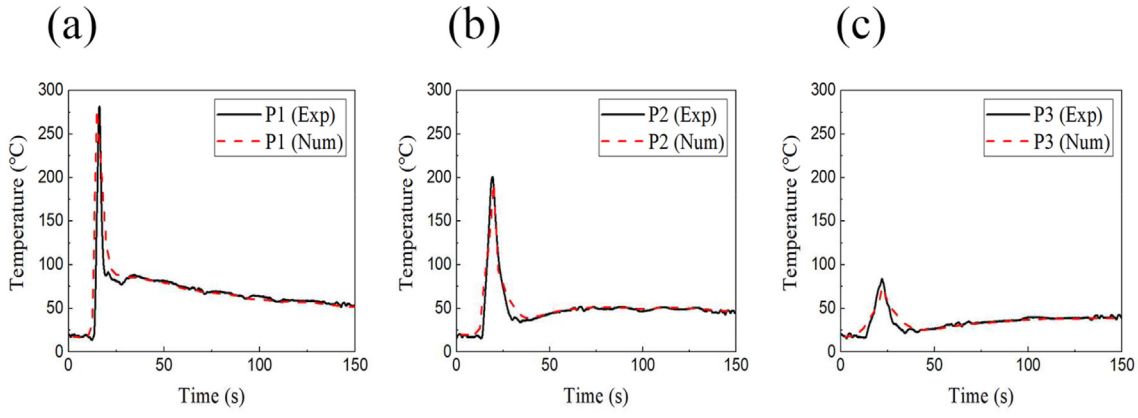

Fig. 12 – Experimental and predicted results of temperature at different measurement points under free convection conditions: (a) P1, (b) P2, (c) P3.

transfer changes from convection to conduction, i.e. more heat is transferred from the as-solidified cladding track by conduction. This numerical model did not capture this feature and can be further improved. But the numerical results are still in good agreement with the measurement with the overall error percentage of 5.83%, 6.29% and 6.88% for P1, P2 and P3, respectively. The developed CFD model can accurately simulate the heat transfer process in laser cladding under extra shielding gas.

The solidification rate R and temperature gradient G at the solidification interface are the two main parameters to influence the solidification microstructure [43]. The cooling rate G*R determines the size of the microstructure. The shape factor G/R determines the morphology of the microstructure.

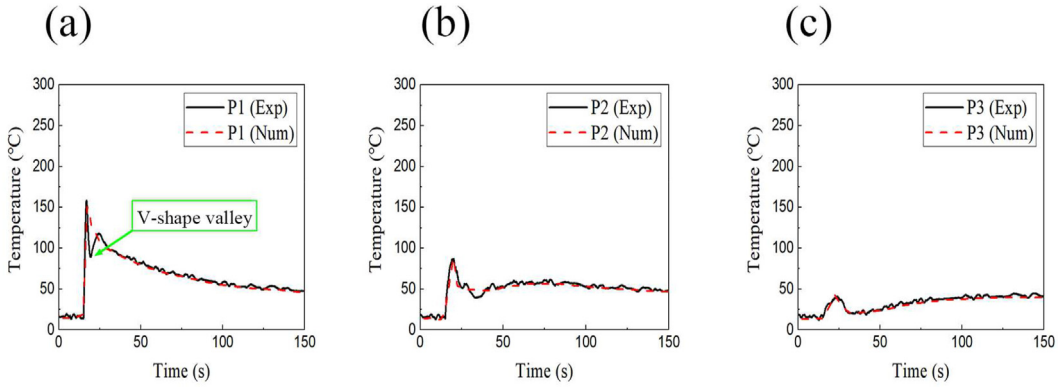

Fig. 13 – Experimental and predicted results of temperature at different measurement points under gas forced convection conditions: (a) P1, (b) P2, (c) P3.

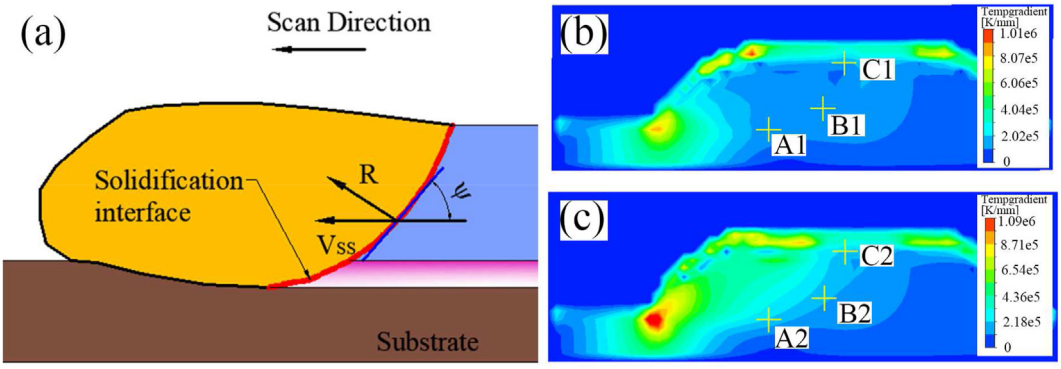

Fig. 14 – (a) The Schematic of molten pool solidification. The simulated temperature gradient distribution of cladding layer: (b) without extra shielding gas; (c) with extra shielding gas.

Table 4 – The temperature gradient and solidification rate of the points in Fig. 14(b).

Location	R(mm/s)	G(K/mm)	G*R(K/s)	G/R
A1	$\begin{bmatrix} R_x \\ R_y \\ R_z \end{bmatrix} = \begin{bmatrix} 6 \\ 0 \\ 2.2 \end{bmatrix}$	$\begin{bmatrix} G_x \\ G_y \\ G_z \end{bmatrix} = \begin{bmatrix} 524 \\ 0.004 \\ 854 \end{bmatrix}$	5022.8	156.8
B1	$\begin{bmatrix} R_x \\ R_y \\ R_z \end{bmatrix} = \begin{bmatrix} 6 \\ 0 \\ 3.7 \end{bmatrix}$	$\begin{bmatrix} G_x \\ G_y \\ G_z \end{bmatrix} = \begin{bmatrix} 366 \\ -0.023 \\ 586 \end{bmatrix}$	4364.2	98.0
C1	$\begin{bmatrix} R_x \\ R_y \\ R_z \end{bmatrix} = \begin{bmatrix} 6 \\ 0 \\ 5.1 \end{bmatrix}$	$\begin{bmatrix} G_x \\ G_y \\ G_z \end{bmatrix} = \begin{bmatrix} 265 \\ -0.026 \\ 403 \end{bmatrix}$	3645.3	61.2

Table 5 – The temperature gradient and solidification rate of the points in Fig. 14(c).

Location	R(mm/s)	G(K/mm)	G*R(K/s)	G/R
A2	$\begin{bmatrix} R_x \\ R_y \\ R_z \end{bmatrix} = \begin{bmatrix} 6 \\ 0 \\ 2.3 \end{bmatrix}$	$\begin{bmatrix} G_x \\ G_y \\ G_z \end{bmatrix} = \begin{bmatrix} 852 \\ -0.043 \\ 1010 \end{bmatrix}$	7435.0	205.6
B2	$\begin{bmatrix} R_x \\ R_y \\ R_z \end{bmatrix} = \begin{bmatrix} 6 \\ 0 \\ 4.1 \end{bmatrix}$	$\begin{bmatrix} G_x \\ G_y \\ G_z \end{bmatrix} = \begin{bmatrix} 645 \\ 0.051 \\ 626 \end{bmatrix}$	6436.6	123.7
C2	$\begin{bmatrix} R_x \\ R_y \\ R_z \end{bmatrix} = \begin{bmatrix} 6 \\ 0 \\ 5.3 \end{bmatrix}$	$\begin{bmatrix} G_x \\ G_y \\ G_z \end{bmatrix} = \begin{bmatrix} 412 \\ 0.107 \\ 869 \end{bmatrix}$	7077.7	120.1

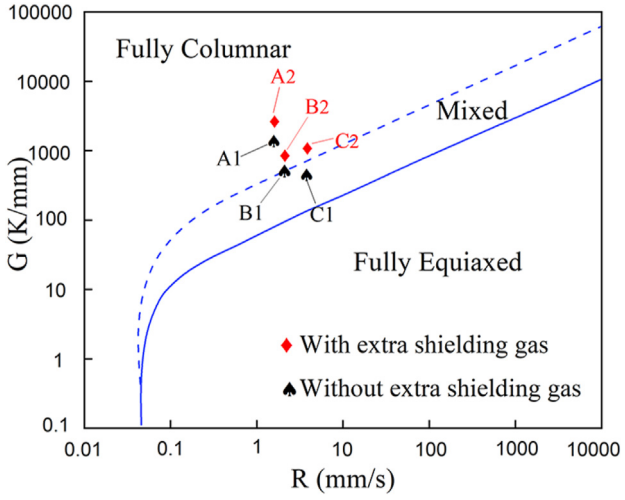

Fig. 15 – Different positions under different laser cladding conditions in solidification map of TC4 alloys [46].

The solidification rate on the liquid-solid interface is related to the scanning speed. Fig. 14(a) illustrates that the direction of solidification rate is always perpendicular to the tangent of the interface. The solidification rate in Z-direction is $V_Z = V_{SS} \cdot \tan\psi$ [25], where V_{SS} is the scanning speed and ψ is the angle subtended by the tangent line and the horizontal line parallel to the scanning direction. This fix cross-section style method was also employed to calculate the solidification rate from the simulation [44,45]. Tables 4 and 5 show the solidification rate and temperature gradient results at the bottom, middle and top of the cladding layer by simulation.

Fig. 15 shows the predicted G and R at different positions of the cladding track in the solidification map of TC4 alloys. The columnar to equiaxed transition (CET) will happen during solidification when the local undercooling is larger than the nucleation undercooling [47]. No CET can occur in the solidification process of laser cladding as shown in Fig. 15. In particular, with the extra shielding gas, the fully columnar region is expected in the entire cladding layer due to the change of solidification parameters.

4.3. *Microstructure and crystallographic textures*

To clarify the relationship between the solidification parameters and microstructure, the microstructure of the corresponding bottom, middle and top parts of the cladding layer was observed in the SEM (Fig. 16).

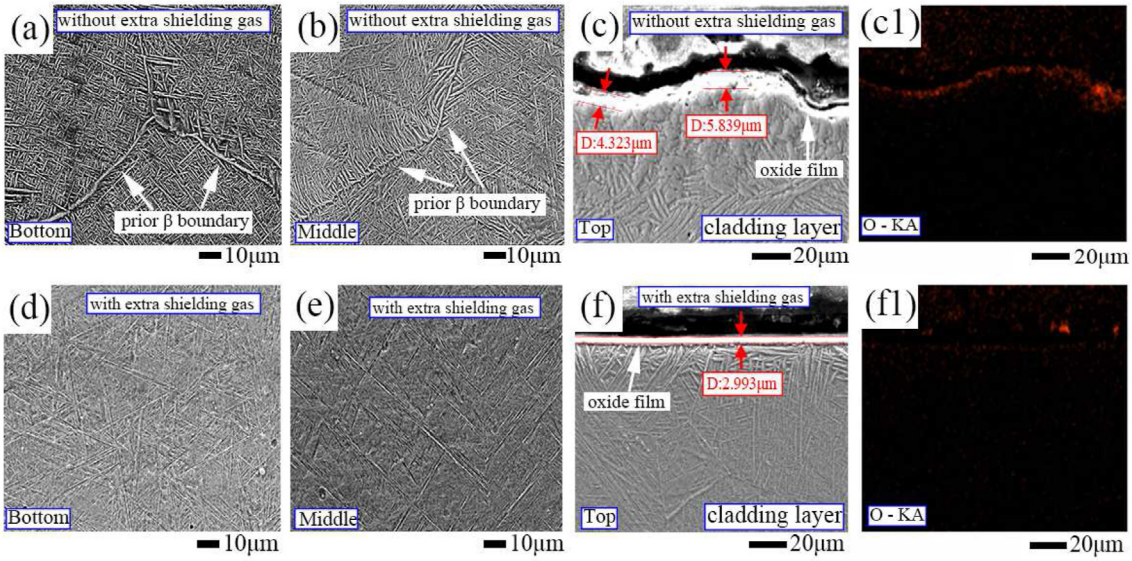

Fig. 16 – The microstructure of cladding track from bottom to top, (a) to (c) without extra shielding gas and (d) to (f) with extra shielding gas. (c1) and (f1) are the EDS results of (c) and (f) at an acceleration voltage of 20 keV.

When the extra shielding gas is not considered, the temperature gradients from the bottom to top of the solidification interface at points A1 (1001.9 K/mm), B1 (690.9 K/mm) and C1 (482.3 K/mm) show the same decreasing trend as the cooling rates at points A1 (5022.8 K/s), B1 (4364.2 K/s) and C1 (3645.3 K/s), as shown in Fig. 14(b) and Table 4. Fig. 16(a) and (b) shows the martensitic α' grains at points A1 and B1, and the prior β grain boundaries can be clearly seen. Fig. 14(c) and Table 5 show that with the extra shielding gas effect, the temperature gradients at points A2 (1321.4 K/mm), B2 (898.8 K/mm) and C2 (961.7 K/mm) are all higher than the gradients without gas effect. The temperature gradient at point C2 (961.7 K/mm) is larger than that in the middle point B2 (898.8 K/mm) due to massive heat dissipation on the surface by the extra gas. Fig. 16(d) and (e) shows that the typical martensitic α' basket-weave microstructure at points A2 and B2.

With the extra shielding gas, the martensitic α' grains become finer especially in the top of the layer due to the faster cooling rate (Fig. 16(c) and (f)). A thin low-oxygen and well-defined oxide film was obtained in both the cladding layers with and without the extra shielding gas. Fig. 16(c1) and (c2) shows the EDS results of (c) and (f), respectively. The oxide

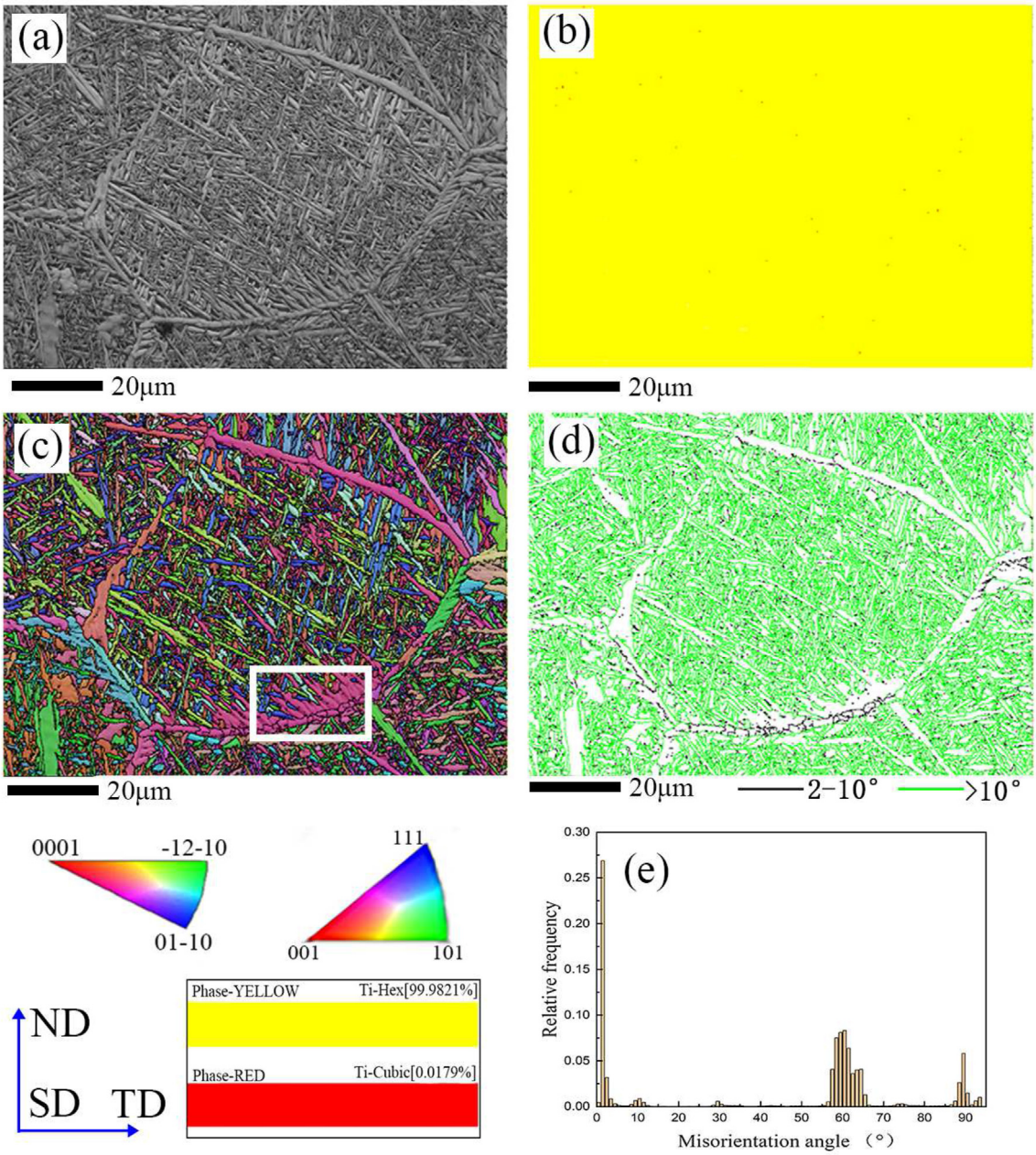

Fig. 17 – The EBSD analysis of cladding layer without extra shielding gas effect: (a) band contrast map, (b) phase map, (c) IPF, (d) grain boundary distribution map and (e) grain boundary histogram.

film of cladding layer in the absence of extra shielding gas consists of massive oxide and is relatively thick, while the extra shielding gas prevents the oxygen from reacting with Ti, resulting in a thinner oxide layer of about 3 μm, as shown in Fig. 16(f).

The Kikuchi patterns are unique to each crystal structure and orientation, and they can be used to determine the crystallographic information. To perform EBSD analysis, the specialized software Channel-5 was used to analyze the Kikuchi pattern of the selected areas. The grain size

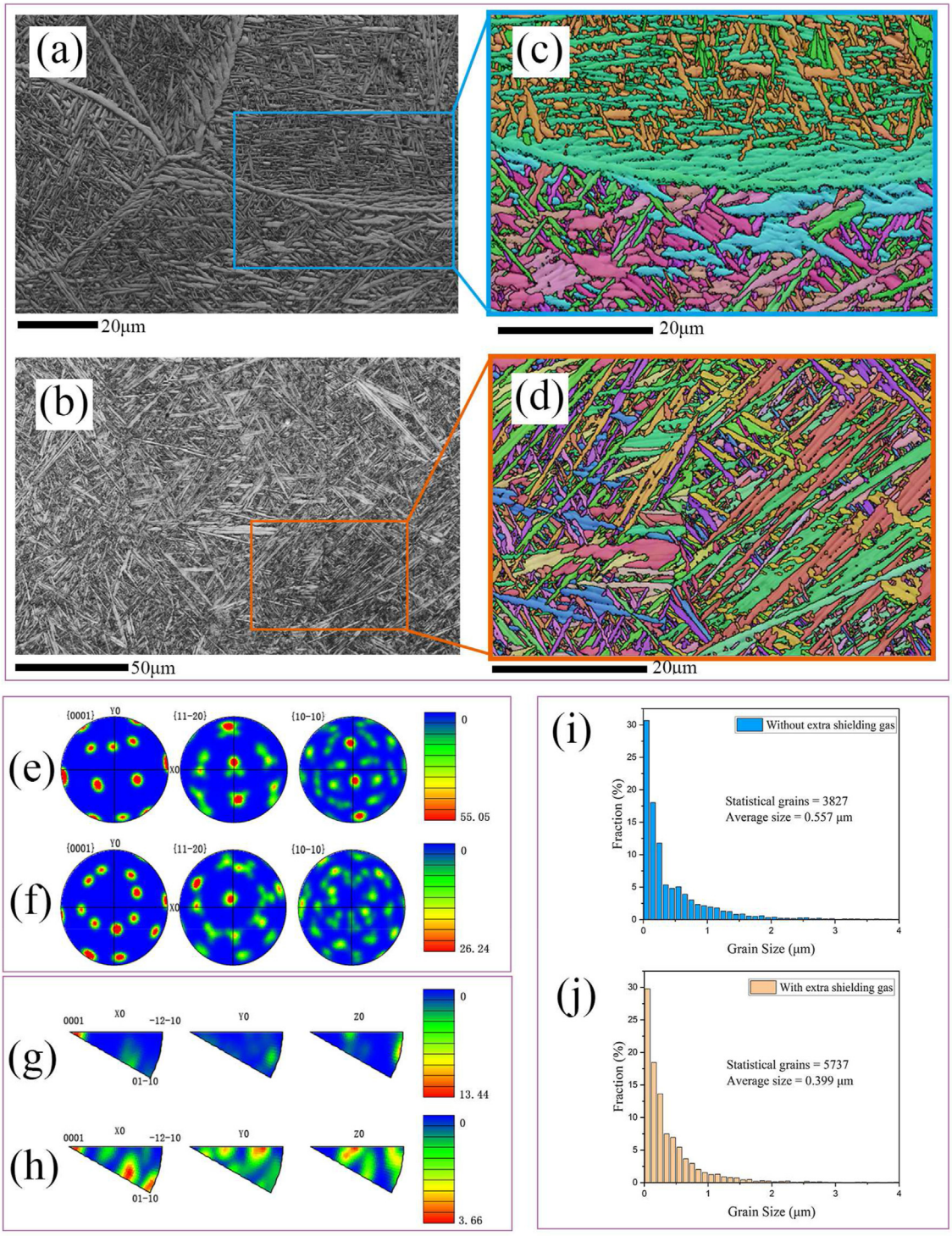

Fig. 18 – The EBSD all Euler maps, pole figures, inverse pole figures and grains statistics analysis of cladding layer: (a), (c), (e), (g), (i) without gas effect and (b), (d), (f), (h), (j) with extra shielding gas.

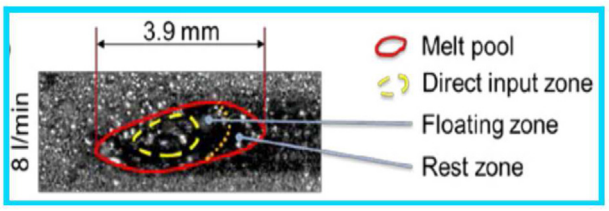

Fig. 19 – Three zones of molten pool [54].

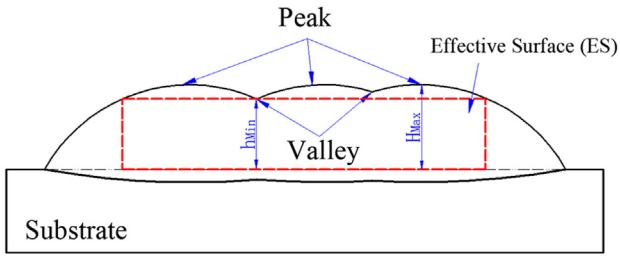

Fig. 21 – Schematic of height and effective surface.

distribution, grain morphology, grain orientation, grain boundary information were analyzed on the samples obtained under different cladding conditions.

Fig. 17 shows the EBSD results of the cladding layer without extra shielding gas. The ND, TD and SD represent the normal, transverse and scanning directions, respectively. The phase map (Fig. 17(b)) shows that the cladding sample is almost all hexagonal α-Ti crystal, reaching a content of 99.9821%. During the cooling process after solidification, the solid-state phase transformation from cubic β-Ti to hexagonal α-Ti occurs in cladding layer. The cooling rate is so high that the martensitic α' phase forms in the majority of the sample in the non-diffusion phase transformation. Because of the crystal characteristics the two types of Ti crystals keep the Burgers, i.e., $\{110\}_{\beta}\|\{0002\}_{\alpha}$ and $<-11-1>_{\beta}\|<2\text{-}1\text{-}10>_{\alpha}$ [48]. Thus, up to 12 crystal equivalent orientation variants may exist during the β to α transition. The presence of multi-variants mitigates the anisotropy of the material. The inverse pole figure (IPF) shows that multiple variants (multiple colors) are present inside the prior β grain, while the similar variants appear near the grain boundary α phase, as shown in the white box in Fig. 17(c). The variant selection caused by grain boundary α phase has a significant impact on the mechanical properties [49,50].

Fig. 17(d) and (e) shows the different angle grain boundaries and statistical histogram of the transformed α phases. The frequencies at the sharp peaks 2°, 10°, 30°, 60° and 90° are similar to the results of Ullah et al. [51]. High angle grain boundaries (HAGBs, >10°) dominate the microstructure. Low angle grain boundaries (LAGBs, 2–10°) mainly occur on the prior β grain boundaries.

During solidification, the α phase preferentially precipitates from the supersaturated β phase to replace the β grain boundaries [52]. Under the gas forced convective heat dissipation by extra shielding gas, the higher cooling rate leaves no time for the grain boundary α phase to precipitate and grow. However, the position of β grain boundary can still be identified as shown in Fig. 18(b) and (d). The LAGBs have lower interfacial energy. Dislocation slip can occur easily near the LAGBs during deformation, and cracks tend to propagate along the LAGBs. Comparing the statistics analyzed in Fig. 18(c) and (d), the fraction of LAGBs decreases from 42.3% to 19.8% under extra shielding gas condition, implying an increase in the strength and fatigue properties of cladding layer. In addition, the statistical results show that the average grain size reduces from 0.557 to 0.399 μm under extra shielding gas condition in Fig. 14(i) and (j), which means the mitigation of property anisotropy [6,53]. Because the hexagonal α-Ti dominates, the pole figure and IPF were analyzed only for this phase. The pole figure results show that the orientation density extremum reaches 55.05 without extra shielding gas, indicating a severe meritocratic orientation in cladding layer. This is mitigated when extra shielding gas is used, and the extremum reduces to 26.24. The IPF shows that a strong texture appears as the extreme value of orientation density reaches 13.44 without gas effect. In contrast, this extreme value drops to 3.66 in the presence of gas effect, implying that no strong textures appear.

4.4. *Surface quality and geometry of cladding layer*

According to Volpp et al. [54], three zones were found in the molten pool by a high speed camera. They are direct input zone, floating zone and rest zone, as shown in Fig. 19. In the direct input zone, the energy is high enough to melt powders immediately. However, unmelted powders float in the vicinity of the direct input zone and even remain at the track surface due to energy attenuation.

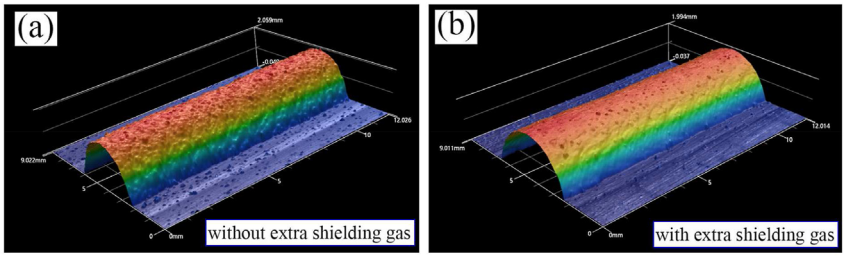

Fig. 20 – The 3D profile of single cladding layer: (a) without extra coaxial shielding gas and (b) with extra coaxial shielding gas.

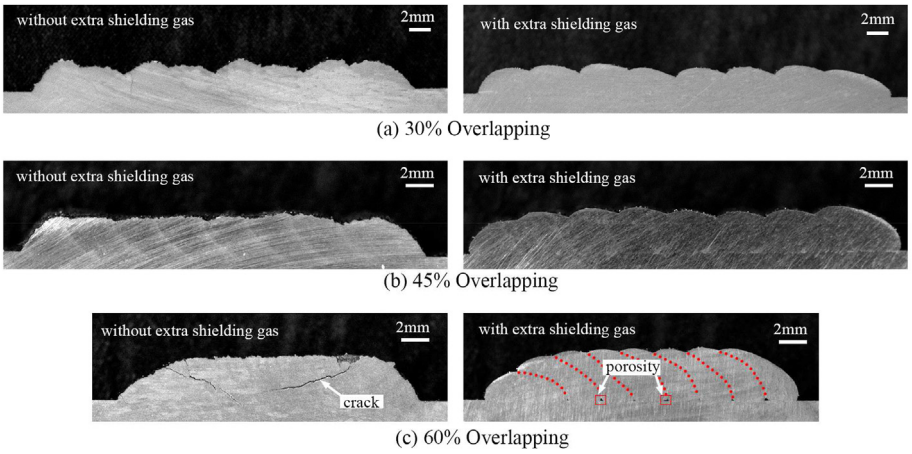

Fig. 22 – Section of overlapping cladding with different overlap ratios: (a) 30%, (b) 45%, (c) 60%.

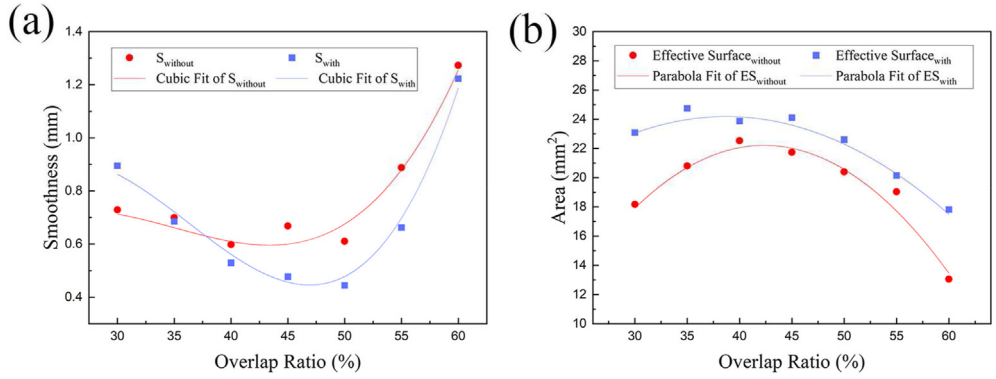

Fig. 23 – The fitting of cladding layer under different overlap ratios: (a) The relative layer flatness S; (b) The effective surface area ES.

Under the simultaneous flattening effect of shielding gas, the increase in surface velocity accelerates the velocity of powders in the floating zone to some extent to compensate for the energy attenuation and promote the surface powder melting. The reduction of unmelted powders on the surface theoretically increases the surface roughness. The 3D macroscopic profile of single cladding layer was characterized by the high-resolution 3D optical profiler, as shown in Fig. 20. It can be pronouncedly seen that a smoother surface of single track was achieved by using extra coaxial shielding gas. The Ra of 18 μm on the cladding layer surface under extra shielding gas (Fig. 20(b)) is lower than that of 21 μm on the surface without extra gas (Fig. 20(a)).

Large area parts are manufactured by multiple cladding steps [55]. In the case of machining-based post-processing, the surface smoothness determines the machining allowance, thereby affecting the machining efficiency [56]. The extra shielding gas effect on geometric profile of the multi-track cladding layers needs to be further investigated. Defining the distance from upper surface of substrate to minimum valley as h_{min} and to maximum peak as H_{max}, the layer flatness of multi-track relative to substrate can be quantified as

$$S = H_{max} - h_{min} \tag{22}$$

In most cases, the cladding layers need to be further processed to meet the service conditions, so h_{min} is taken as the height and a rectangular area can represent the maximum effective surface, as shown in Fig. 21.

The overlap ratio ε of adjacent tracks is the main factor to dimensional accuracy, surface quality and mechanical performance [57]. To investigate the extra shielding gas effect on the surface morphology of multi-track cladding layers, 7 levels

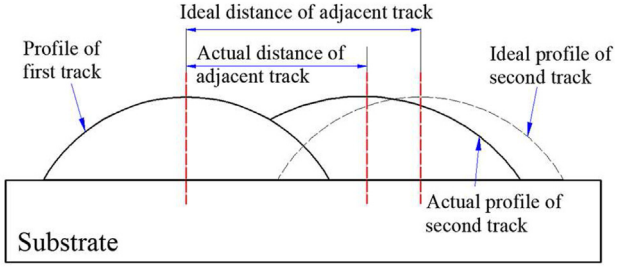

Fig. 24 – The schematic diagram of the center shift effect.

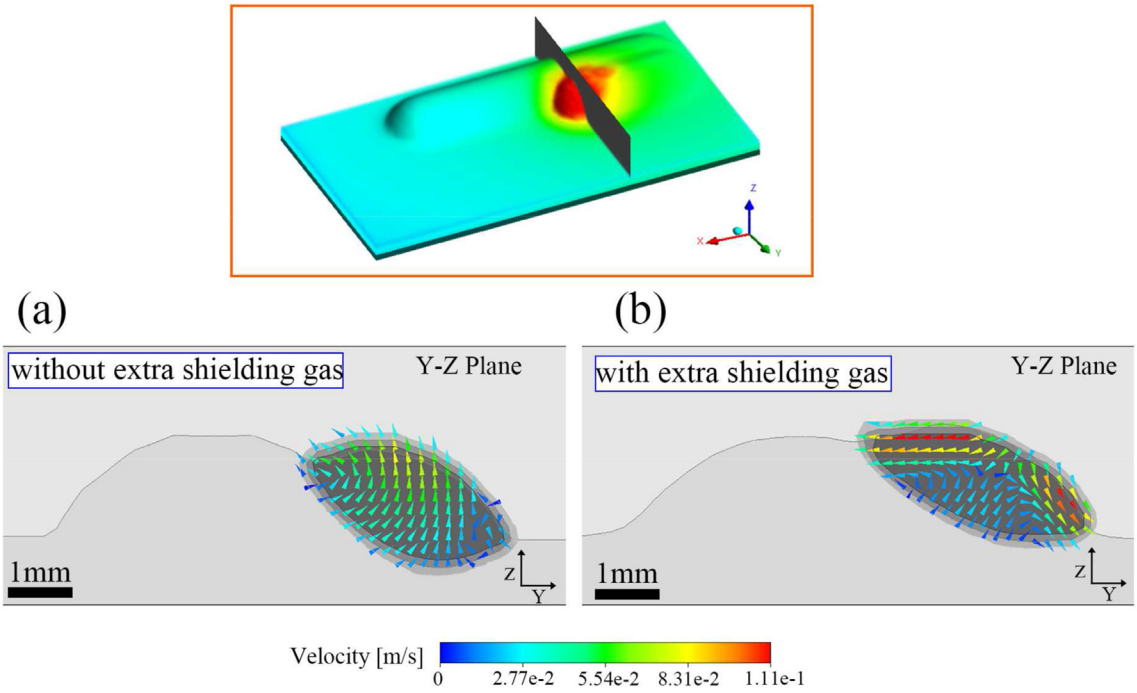

Fig. 25 – The velocity simulation results on Y-Z Plane of liquid molten pool of overlap track: (a) without extra shielding gas; (b) with extra shielding gas.

of overlap ratios distributed uniformly from 30% to 60% were taken to clad 8 tracks. The different overlap ratios imply different heat transfer conditions and further represent different residual stress [58]. The cracks appeared with the overlap ratio larger than 50% under as-received condition due to higher residual stress by intensive repeated heat treatment. However, in the presence of extra shielding gas, no cracks appear under all the tested overlap ratio (30%–60%). This is also due to the reduction of the LAGBs, which improves the crack resistance, as described in Section 4.3. Notably, the acceleration of heat dissipation leads to inter-run porosities due to a lack of fusion (LOF) [59] when the overlap ratio reaches 60%, as shown in Fig. 22(c). This can be explained by the fact that the increase of tangential angle of the track outline at the overlapping zone decreases the laser energy absorption [60].

Fig. 23 plots the relative layer flatness S and effective surface area ES as a function of overlap ratio ε. As shown in Fig. 23(a), with an overlap ratio >35%, the S with extra shielding gas is lower than the as-received cladding. This indicates that the extra shielding gas can flatten the multi-track layers in a wide range of overlapping ratio. Overall, the waves are less pronounced without extra shielding gas effect due to the bonding of unmelted powders on surface (Fig. 22). However, the ES values (Fig. 23(b)) show that the bunching effect of extra shielding gas leads to a larger ES, indicating an increase in powder utilization efficiency.

Theoretically, the multi-track cladding layer consists of uniform single tracks. However, compared to the first cladding layer, the powder feeding of the subsequent cladding layers could be affected by the blocking effect of the previous cladding layers, which may further lead to a change in powder utilization. In addition to the melting of feed powders, part of the existing neighboring track is remelted to form the multi-track [61]. The overlap part can make the upper surface flatter by lifting the surface valley, but the center of the new track can be shifted [62], as shown in Fig. 24. In laser cladding of multiple tracks, the overlap ratio ε is defined by first track, and the accumulated offsets cause the real subsequent overlap ratio to deviate from the defined value. Fig. 25 illustrates the simulation results of molten pool of overlap track cladding. With the extra shielding gas, the velocity on the molten pool surface increases and the liquid flows to the valley, leading to a flatter surface and moderating the shift center of the track.

5. Summary and conclusions

A computational fluid dynamic (CFD) model using the Volume-of-Fluid (VOF) method was established to simulate the laser cladding process with coaxial shroud protection and investigate the extra shielding gas effect on the molten pool. The gas impulse condition and gas forced convection condition were applied on the free surface in the model. Based on the numerical simulation and experimental results, the conclusions are summarized as follows:

(1) The numerical simulation results reveal the flow and thermal characteristics of molten pool. The extra shielding gas increases the velocity near the molten pool surface, which compensates for the energy attenuation and promotes the surface powder

melting. The simulated solidification parameters imply that the microstructure in the cladding layer is fully columnar under higher cooling rate due to the extra shielding gas.

(2) A thin and uniform oxide film of about 3 μm thickness can be obtained with the application of extra shielding gas. The high cooling rate inhibits the appearance of grain boundary α phase and reduces the fraction of low angle grain boundaries from 42.3% to 19.8%. The grains are refined from 0.557 to 0.399 μm. This implies an increase in strength and potentially mitigates the anisotropy of cladding layers.

(3) In the presence of extra shielding gas, the surface roughness Ra of cladding layers is reduced from 21 to 18 μm due to shielding gas flattening effect and the surface velocity acceleration on the powder velocity in the floating zone. The massive heat loss due to extra shielding gas significantly reduces crack formation in multi-track cladding with a large overlap ratio, but inter-run porosity will occur when the overlap ratio is 60% or more. Meanwhile, the bunching effect of shielding gas increases the powder utilization efficiency.

Credit authorship contribution statement

Peijie Lyu: Conceptualization, Methodology, Validation, Visualization, Formal analysis, Software, Investigation, Data curation, Writing – original draft. **Peifeng Li:** Conceptualization, Supervision, Writing – review & editing. **Kaiyong Jiang:** Conceptualization, Supervision, Resources, Funding acquisition.

Declaration of competing interest

The authors declare that they have no known competing financial interests or personal relationships that could have appeared to influence the work reported in this paper.

Acknowledgment

This work was supported by National Natural Science Foundation of China [51475174] and Subsidized Project for Postgraduates' Innovative Fund in Scientific Research of Huaqiao University.

REFERENCES

[1] Toyserkani E, Khajepour A, Corbin SF. Laser cladding. Boca Raton(FL): CRC Press; 2004.
[2] Thompson SM, Bian L, Shamsaei N, Yadollahi A. An overview of Direct Laser Deposition for additive manufacturing; Part I: transport phenomena, modeling and diagnostics. Addit Manuf 2015;8:36–62.
[3] Lee C, Woo W, Roh Y. Remanufacturing: trends and issues. Int J Precision Eng and Manufacturing-Green Technol 2017;4(1):113–25.
[4] Chen Y, Chen X, Jiang M, Lei Z, Wang Z, Liang J, et al. Coaxial laser metal wire deposition of Ti6Al4V alloy: process, microstructure and mechanical properties. J Mater Res Technol 2022;20:2578–90.
[5] He X, Song L, Yu G, Mazumder J. Solute transport and composition profile during direct metal deposition with coaxial powder injection. Appl Surf Sci 2011;258(2):898–907.
[6] Yang Z, Wang S, Zhu L, Ning J, Xin B, Dun Y, et al. Manipulating molten pool dynamics during metal 3D printing by ultrasound. Appl Phys Rev 2022;9:021416.
[7] Siao Y, Wen C. Examination of molten pool with Marangoni flow and evaporation effect by simulation and experiment in selective laser melting. Int Commun Heat Mass Tran 2021;125(4):105325.
[8] Zhang Y, Lim C, Tang C, Li B. Numerical investigation on heat transfer of melt pool and clad generation in directed energy deposition of stainless steel. Int J Therm Sci 2021;165(2):106954.
[9] Li C, Yu Z, Gao J, Zhao J, Han X. Numerical simulation and experimental study of cladding Fe60 on an ASTM 1045 substrate by laser cladding. Surf Coating Technol 2019;357:965–77.
[10] Arrizubieta JI, Lamikiz A, Cortina M, Ukar E, Alberdi A. Hardness, grainsize and porosity formation prediction on the Laser Metal Deposition of AISI 304 stainless steel. Int J Mach Tool Manufact 2018;135:53–64.
[11] Farahmand P, Kovacevic R. Laser cladding assisted with an induction heater (LCAIH) of Ni–60%WC coating. J Mater Process Technol 2015;222:244–58.
[12] Wen S, Shin Y. Modeling of transport phenomena during the coaxial laser direct deposition process. J Appl Phys 2010;108(4):044908.
[13] Yang J, Aiyiti W, Jiang H, Shan J, Zhang Y. Evolution of molten pool morphology and prediction of inclined cladding layer morphology. Opt Laser Technol 2021;142:107164.
[14] Zhang H, Kong F, Wang G, Zeng L. Numerical simulation of multiphase transient field during plasma deposition manufacturing. J Appl Phys 2006;100(12):123522.
[15] Poprawe R. Tailored light 2: laser application technology. Aachen: Springer Verlag; 2011.
[16] Lyu P, Jin L, Yan B, Zhu L, Yao J, Jiang K. Numerical simulation and experimental investigation of the effect of three-layer annular coaxial shroud on gas-powder flow in laser cladding. J Manuf Process 2022;84:457–68.
[17] Chen L, Zhao Y, Song B, Yu T, Liu Z. Modeling and simulation of 3D geometry prediction and dynamic solidification behavior of Fe-based coatings by laser cladding. Opt Laser Technol 2021;139:107009.
[18] Song B, Yu T, Jiang X, Xi W, Lin X. The relationship between convection mechanism and solidification structure of the iron-based molten pool in metal laser direct deposition. Int J Mech Sci 2020;165:105207.
[19] Khamidullin BA, Tsivilskiy IV, Gorunov AI, Gilmutdinov AK. Modeling of the effect of powder parameters on laser cladding using coaxial nozzle. Surf Coating Technol 2019;364:430–43.
[20] Xu W, Lui EW, Pateras A, Qian M, Brandt M. In situ tailoring microstructure in additively manufactured Ti-6Al-4V for superior mechanical performance. Acta Mater 2017;125:390–400.
[21] Haldar B, Saha P. Identifying defects and problems in laser cladding and suggestions of some remedies for the same. Mater Today Proc 2018;5(5):13090–101. Part 2.
[22] Bakir N, Gumenyuk A, Rethmeier M. Investigation of solidification cracking susceptibility of laser welded joints of

austenitic stainless steels, Welding and failure analysis of engineering materials. Luxor, Egypt: WAFA-2015); 2015. A-29, 1-A-29, 9.
[23] Korsmik R, Klimova-Korsmik O, Valdaytseva E, Udin I. Investigation of cracking causes during multi-pass laser cladding of heat-resistant single crystal nickel alloy. Procedia CIRP 2020;94:314–9.
[24] Alhendal Y, Turan A. Volume-of-Fluid (VOF) simulations of Marangoni bubbles motion in zero gravity. Finite Volume Method - Powerful Means of Engineering Design; 2012.
[25] Song J, Chew Y, Bi G, Yao X, Zhang B, Bai J, et al. Numerical and experimental study of laser aided additive manufacturing for melt-pool profile and grain orientation analysis. Mater Des 2018;137:286–97.
[26] Gao J, Wu C, Liang X, Hao Y, Zhao K. Numerical simulation and experimental investigation of the influence of process parameters on gas-powder flow in laser metal deposition. Opt Laser Technol 2020;125(1–2):106009.
[27] Lu X, Lin X, Chiumenti M, Cervera M, Hu Y, Ji X, et al. In situ measurements and thermo-mechanical simulation of Ti–6Al–4V laser solid forming processes. Int J Mech Sci 2019;153–154:119–30.
[28] Gouge M. Chapter 3 - convection boundary losses during laser cladding. In: Gouge M, Michaleris P, editors. Thermo-mechanical modeling of additive manufacturing. Butterworth-Heinemann; 2018. p. 41–60.
[29] Gouge MF, Heigel JC, Michaleris P, Palmer TA. Modeling forced convection in the thermal simulation of laser cladding processes. Int J Adv Des Manuf Technol 2015;79(1):307–20.
[30] Hao M, Sun Y. A FEM model for simulating temperature field in coaxial laser cladding of TI6AL4V alloy using an inverse modeling approach. Int J Heat Mass Tran 2013;64:352–60.
[31] Brackbill JU, Kothe DB, Zemach C. A continuum method for modeling surface tension. J Comput Phys 1992;100(2):335–54.
[32] Saldi ZS. Marangoni driven free surface flows in liquid weld pools. Delft University of Technology; 2012.
[33] Abramovich GN. The theory of turbulent jets. MIT Press; 2003.
[34] Tan H, Zhang F, Fu X, Meng J, Hu G, Fan W, et al. Development of powder flow model of laser solid forming by analysis method. Int J Adv Des Manuf Technol 2016;82(5):1421–31.
[35] Zhong C, Pirch N, Gasser A, Poprawe R, Schleifenbaum JH. The influence of the powder stream on high-deposition-rate laser metal deposition with inconel 718. Metals 2017;7(10):443.
[36] Pauzon C, Dietrich K, Forêt P, Hryha E, Witt G. Mitigating oxygen pick-up during laser powder bed fusion of Ti-6Al-4V by limiting heat accumulation. Mater Lett 2021;288:129365.
[37] Chen M, Lu Y, Wang Z, Lan H, Sun G, Ni Z. Melt pool evolution on inclined NV E690 steel plates during laser direct metal deposition. Opt Laser Technol 2021;136:106745.
[38] Guo Q, Zhao C, Qu M, Xiong L, Hojjatzadeh SMH, Escano LI, et al. In-situ full-field mapping of melt flow dynamics in laser metal additive manufacturing. Addit Manuf 2020;31:100939.
[39] Chen L, Yu T, Xu P, Zhang B. In-situ NbC reinforced Fe-based coating by laser cladding: simulation and experiment. Surf Coating Technol 2021;412:127027.
[40] Ge H, Xu H, Wang J, Li J, Yao J. Investigation on composition distribution of dissimilar laser cladding process using a three-phase model. Int J Heat Mass Tran 2021;170:120975.
[41] Gao W, Zhao S, Wang Y, Zhang Z, Liu F, Lin X. Numerical simulation of thermal field and Fe-based coating doped Ti. Int J Heat Mass Tran 2016;92:83–90.
[42] Heigel JC, Michaleris P, Reutzel EW. Thermo-mechanical model development and validation of directed energy deposition additive manufacturing of Ti–6Al–4V. Addit Manuf 2015;5:9–19.
[43] Boettinger WJ, Banerjee DK. Solidification. In: Laughlin DE, Hono K, editors. Physical Metallurgy. fifth ed. Oxford: Elsevier; 2014. p. 639–850.
[44] Gao S, Feng Y, Wang J, Qin M, Bodunde OP, Liao W-H, et al. Molten pool characteristics of a nickel-titanium shape memory alloy for directed energy deposition. Opt Laser Technol 2021;142:107215.
[45] Zhao Y, Koizumi Y, Aoyagi K, Wei D, Yamanaka K, Chiba A. Molten pool behavior and effect of fluid flow on solidification conditions in selective electron beam melting (SEBM) of a biomedical Co-Cr-Mo alloy. Addit Manuf 2019;26:202–14.
[46] Zhang G, Lu X, Li J, Chen J, Lin X, Wang M, et al. In-situ grain structure control in directed energy deposition of Ti6Al4V. Addit Manuf 2022;55:102865.
[47] Lin X, Li Y, Meng W, Feng L, Chen J, Huang W. Columnar to equiaxed transition during alloy solidification. Science in China(Series E:Technological Sciences) 2003;(5):475–89.
[48] Obasi G, Birosca S, Da Fonseca JQ, Preuss M. Effect of β grain growth on variant selection and texture memory effect during α→ β→ α phase transformation in Ti–6 Al–4 V. Acta Mater 2012;60(3):1048–58.
[49] Lütjering G, Williams JC. Titanium matrix composites. Springer; 2007.
[50] Stanford N, Bate P. Crystallographic variant selection in Ti–6Al–4V. Acta Mater 2004;52(17):5215–24.
[51] Ullah R, Lu J, Sang L, Rizwan M, Zhang Y, Zhang Z. Investigating the microstructural evolution during deformation of laser additive manufactured Ti–6Al–4V at 400° C using in-situ EBSD. Mater Sci Eng, A 2021;823:141761.
[52] Sun Z, Li X, Wu H, Yang H. A unified growth model of the secondary grain boundary α phase in TA15 Ti-alloy. J Alloys Compd 2016;689:693–701.
[53] Martin JH, Yahata BD, Hundley JM, Mayer JA, Schaedler TA, Pollock TM. 3D printing of high-strength aluminium alloys. Nature 2017;549(7672):365–9.
[54] Volpp J, Prasad HS, Riede M, Brueckner F, Kaplan AFH. Powder particle attachment mechanisms onto liquid material. Procedia CIRP 2018;74:140–3.
[55] de Oliveira U, Ocelík V, De Hosson JTM. Analysis of coaxial laser cladding processing conditions. Surf Coating Technol 2005;197(2):127–36.
[56] Zhu L, Wang S, Lu H, Qi D, Wang D, Yang Z, et al. Investigation on synergism between additive and subtractive manufacturing for curved thin-walled structure. Virtual Phys Prototyp 2022;17(2):220–38.
[57] Chen C, Lian G, Jiang J, Wang Q. Simplification and experimental investigation of geometrical surface smoothness model for multi-track laser cladding processes. J Manuf Process 2018;36:621–8.
[58] Cao J, Liu F, Lin X, Huang C, Chen J, Huang W. Effect of overlap rate on recrystallization behaviors of Laser Solid Formed Inconel 718 superalloy. Opt Laser Technol 2013;45:228–35.
[59] Paul CP, Mishra SK, Kumar A, Kukreja LM. Laser rapid manufacturing on vertical surfaces: analytical and experimental studies. Surf Coating Technol 2013;224:18–28.
[60] Wang S, Ning J, Zhu L, Yang Z, Yan W, Dun Y, et al. Role of porosity defects in metal 3D printing: formation mechanisms, impacts on properties and mitigation strategies. Mater Today 2022;59:133–60.
[61] Sun S, Brandt M, Harris J, Durandet Y. The influence of stellite 6 particle size on the inter-track porosity in multi-track cladding. Surf Coating Technol 2006;201(3):998–1005.
[62] Li Y, Sun Y, Han Q, Zhang G, Horváth I. Enhanced beads overlapping model for wire and arc additive manufacturing of multi-layer multi-bead metallic parts. J Mater Process Technol 2018;252:838–48.